

Quantum anomalous Hall effects and Hall crystals at fractional filling of helical trilayer graphene

Sen Niu,^{1,*} Jason Alicea,^{2,†} D. N. Sheng,^{1,‡} and Yang Peng^{1,2,§}

¹*Department of Physics and Astronomy, California State University Northridge, California 91330, USA*

²*Institute of Quantum Information and Matter and Department of Physics,
California Institute of Technology, Pasadena, CA 91125, USA*

(Dated: June 6, 2025)

Helical trilayer graphene realizes a versatile moiré system in which anomalous Hall effects have been recently observed at integer and fractional fillings. Focusing on helical trilayers near the magic angle and under a substrate potential, we demonstrate that an isolated higher Chern band with Chern number $|C_{band}| = 2$ emerges, enabling the exploration of many-body states beyond the conventional Landau level paradigm. We use exact diagonalization to predict a rich phase diagram of gapped states unattainable in a single $|C_{band}| = 1$ band. At filling $\nu = 2/3$, we identify a quantum Hall crystal with integer Hall conductance $|\sigma_H| = e^2/h$ coexisting with a $\sqrt{3} \times \sqrt{3}$ charge density wave order. At $\nu = 1/2$, we find a quantum Hall pseudospin ferromagnet featuring extensive ground state degeneracy, Hall conductance $|\sigma_H| = e^2/h$, and 2×2 charge order. Finally, at $\nu = 1/3$ we find a translation-symmetric fractional Chern insulator with $|\sigma_H| = 2e^2/3h$. By incorporating spin and valley degrees of freedom, we identify an optimal filling regime $\nu_{total} = 3 + \nu$, where three flavors are fully filled, leaving the fourth at partial filling ν . Notably, inter-flavor interactions renormalize the bandwidth and stabilize all the gapped phases even in realistic parameter regimes away from the chiral limit.

Introduction. Moiré superlattices, engineered to host flat topological electronic bands with dramatically enhanced electron-electron interactions, have emerged as a versatile platform to explore correlated topological phases [1, 2]. One of the major breakthroughs in this field is the observation of zero-field fractional Chern insulators [3–7] (FCIs) in twisted transition metal dichalcogenides (TMDs) [8–11] and rhombohedral pentalayer graphene/hBN moiré superlattices [12], paving a new route toward anyon-based quantum devices. The phenomenology has been enriched further still by the discovery of quantum Hall crystals (QHCs)—which exhibit quantized Hall conductance alongside charge density wave (CDW) order [13–22]—in various graphene multilayers [23–26].

Moiré systems feature exquisitely tunable electronic structure via changes in twist angle and number of layers. Helical trilayer graphene (HTG), composed of three layers of graphene with successive twist angles θ , displays a supermoiré structure on length scale $1/\theta^2$ forming symmetry-related domains [27] as well as a finer moiré pattern on a $1/\theta$ length scale [28–32]. Within individual domains, the system hosts degenerate $C_{band} = \pm 1, \mp 2$ Chern bands separated from remote bands [29–31]. Experimental observations of anomalous Hall effects at integer fillings confirm the existence of these Chern bands, yet the nature of correlated states at fractional fillings $\nu = 2/3, 7/2$ remains unresolved [33]. Recent theoretical studies have also proposed mechanisms for correlated states in HTG [34], including Laughlin-type FCIs stabilized in an isolated $|C_{band}| = 1$ band [35]. The higher $|C_{band}| = 2$ Chern band is especially intriguing, as it may support exotic correlated Hall states unattainable in a single Landau-level-like band [36–39]. In particular, Halperin-type FCIs and quantum Hall ferromagnets (QHF) have been systematically constructed in the chiral limit of higher Chern bands with ideal quantum geometry [40]. These developments raise several important questions for HTG: Can the aforementioned phases be stabilized in realistic material beyond the

chiral limit? What are the optimal parameter regimes for realization of these correlated states? Addressing these questions will enhance our understanding of current experimental observations and guide future explorations.

In this letter, we investigate correlated states in the higher Chern band of HTG. Close to the magic angle, we show that the $|C_{band}| = 2$ band can be energetically decoupled from other bands [Fig. 1 (a)] using substrate-induced sublattice potentials. Through extensive exact diagonalization, we uncover a rich phase diagram [Fig. 1 (c)] including a K point QHC at $\nu = 2/3$, a QHF at $\nu = 1/2$ with M point charge order, and a Halperin-type FCI at $\nu = 1/3$. These states have distinct quantized Hall conductances and their unique charge orders which can be identified via momentum space and real space correlation functions. While a single-particle kinetic energy nontrivially competes with the Coulomb interaction under non-chiral conditions, inter-flavor (spin/valley) interactions induce a bandwidth renormalization at filling $\nu_{total} = 3 + \nu$ when three flavors are fully occupied and the remaining flavor is partially filled [Fig. 1 (b)]—effectively enhancing interactions and stabilizing gapped many-body states at realistic parameter regimes.

Higher Chern band and many-body Hamiltonian. The helical trilayer Hamiltonian for a single flavor (spin and valley) takes the form [29–31]

$$H_0 = \begin{pmatrix} \hbar v_0 \hat{\mathbf{k}} \cdot \boldsymbol{\sigma} & T(\mathbf{r}, \Phi) & 0 \\ h.c. & \hbar v_0 \hat{\mathbf{k}} \cdot \boldsymbol{\sigma} & T(\mathbf{r}, -\Phi) \\ 0 & h.c. & \hbar v_0 \hat{\mathbf{k}} \cdot \boldsymbol{\sigma} \end{pmatrix}, \quad (1)$$

where $\sigma_{x,y,z}$ act on A/B sublattices, $\hat{\mathbf{k}} = (V k_x, k_y - V K_y^j)$ is layer-dependent momentum center with $V = \mp 1$ labeling the K, K' valleys, and $K_y^j = (j - 2)k_\theta$ represents the momentum shifts for three layers $j = 1, 2, 3$. Throughout we assume Fermi velocity $v_0 = 10^6$ m/s, moiré lattice spacing $a_M = a_0/2 \sin \frac{\theta}{2}$ with graphene lattice constant $a_0 = 2.46 \text{ \AA}$, and reciprocal wavevector $k_\theta = 4\pi/3a_M$. The tun-

neling potential $T(\mathbf{r}, \Phi)$ for K valley [$T(\mathbf{r}, \Phi)^\dagger$ for K' valley] takes the form $T(\mathbf{r}, \Phi) = \sum_n T_n e^{-i\Phi_n} e^{-i\mathbf{q}_n \cdot \mathbf{r}}$, where the tunneling matrices T_n are defined as $T_n = w_{AA}\sigma_0 + w_{AB}[\sigma_x \cos \frac{2\pi(n-1)}{3} - \sigma_y \sin \frac{2\pi(n-1)}{3}]$ with $w_{AB} = 110$ meV. The momentum vectors are $\mathbf{q}_1 = k_\theta(0, -1)$, $\mathbf{q}_2 = k_\theta(\sqrt{3}/2, 1/2)$, $\mathbf{q}_3 = k_\theta(-\sqrt{3}/2, 1/2)$, and the inter-layer offset $\Phi = \frac{2\pi}{3}(0, 1, -1)$ is fixed as a constant inside a domain [29, 30].

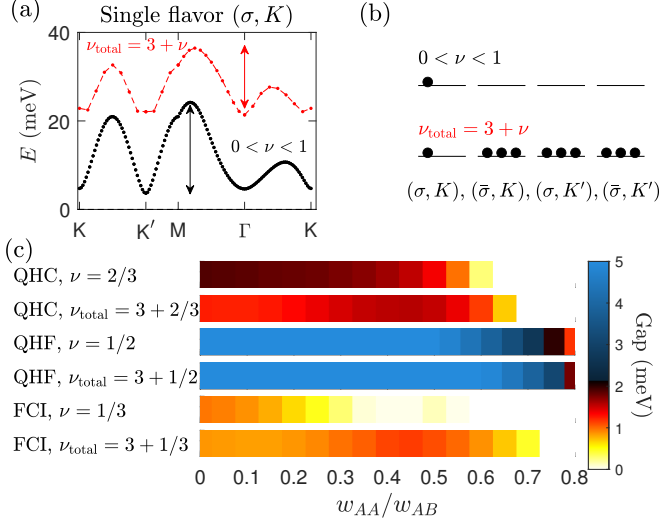


FIG. 1. Chern bands and qualitative many-body phase diagrams. (a) Single-particle Chern bands (black curve) with $C_{\text{band}} = -2$ and mean-field renormalized dispersion (red curve) for $w_{AA}/w_{AB} = 0.6$. (b) Schematic flavor polarization at two filling regimes. (c) Phase diagrams for quantum Hall crystal (QHC), quantum Hall ferromagnet (QHF) and fractional Chern insulator (FCI) states at filling regimes $0 < \nu < 1$ and $\nu_{\text{total}} = 3 + \nu$. Results for $\nu = 2/3, 1/2, 1/3$ are obtained on $N_s = 27, 28, 24$ clusters, respectively.

In the chiral limit ($\omega_{AA} = 0.0$) and at the magic angle $\theta = 1.5^\circ$, HTG exhibits two exactly flat, degenerate central bands carrying a total Chern number -1 for the K valley ($+1$ for K'). When expressed in the sublattice-polarized basis, these split into one band that mimics a single Landau level with $C_{\text{band}} = 1$ and another higher Chern band with $C_{\text{band}} = -2$ [29, 30]. To energetically separate the two bands, we consider an external sublattice potential $H_\mu = \text{diag}(\mu_1\sigma_z, \mu_2\sigma_z, \mu_3\sigma_z)$ which can be induced by alignment to a hexagonal boron nitride (hBN) substrate [41]. In the idealized case $\mu_1 = \mu_2 = \mu_3$, the two bands split rigidly without modifying their dispersions. Here we choose $\mu = (-4, -6, -8)$ meV, reflecting a decaying hBN-induced potential from bottom to top layer. For this study, we fix the twist angle at $\theta = 1.44^\circ$ (near the magic angle) and use $w_{AA} = 0.6w_{AB}$ to model realistic corrugation. Due to the μ potential, the non-interacting $C_{\text{band}} = -2$ band acquires positive kinetic energy as shown in Fig. 1 (a), separated from the negative energy $C_{\text{band}} = +1$ band. More details for substrate effects on band structures can be found in Supplemental Material (SM). Crucially, deviations from the chiral limit de-

stroy band flatness, inducing the competing kinetic energy that influences correlated phases.

Let us now project onto the single $C_{\text{band}} = -2$ band, treating the charge neutrality point (occupied negative-energy bands) as the vacuum. The projected Coulomb interaction [42] reads

$$H_{\text{int}} = \frac{1}{2A} \sum_{\beta_1, 2, 3, 4} \sum_{\mathbf{k}_1, \mathbf{k}_2, \mathbf{q}} V_{\beta_1, \beta_2, \beta_3, \beta_4}(\mathbf{k}_1, \mathbf{k}_2, \mathbf{q}) \times \psi_{\beta_1, \mathbf{k}_1}^\dagger \psi_{\beta_2, \mathbf{k}_2}^\dagger \psi_{\beta_3, [\mathbf{k}_2 - \mathbf{q}]} \psi_{\beta_4, [\mathbf{k}_1 + \mathbf{q}]}, \quad (2)$$

where $\psi_{\beta, \mathbf{k}}$ corresponds to the Bloch basis obtained from diagonalizing Eq. (1); flavor $\beta_i = (\sigma_i, V_i)$ labels spin and valley degrees of freedom; and $A = \frac{8\pi^2 N_s}{3\sqrt{3}k_\theta^2}$ is the system area with N_s moiré cells. The momentum sum is restricted to the moiré first Brillouin zone (FBZ), with $[\cdot]$ indicating momentum reduction to the FBZ via reciprocal lattice vector shifts. The interaction matrix element is related to the form factor via $V_{\beta_1, \beta_2, \beta_3, \beta_4}(\mathbf{k}_1, \mathbf{k}_2, \mathbf{q}) = V(\mathbf{q}) \langle \beta_1, \mathbf{k}_1 | e^{-i\mathbf{q} \cdot \mathbf{r}} | \beta_4, [\mathbf{k}_1 + \mathbf{q}] \rangle \langle \beta_2, \mathbf{k}_2 | e^{i\mathbf{q} \cdot \mathbf{r}} | \beta_3, [\mathbf{k}_2 - \mathbf{q}] \rangle$. Here $V(\mathbf{q}) = \frac{2\pi e^2 k_0}{|\mathbf{q}| \epsilon} (1 - \delta_{\mathbf{q}, 0})$ is the Coulomb potential with k_0 being the Coulomb constant, and the dielectric constant is fixed to $\epsilon = 4$.

Coulomb interactions in twisted graphene can lift the four-fold flavor degeneracy of Chern bands [33–35, 43–45]. Focusing on the $C_{\text{band}} = -2$ band, we consider two distinct regimes of flavor polarizations as illustrated in Fig. 1 (b). Case (i): For $0 < \nu < 1$, only one flavor $\beta = (\sigma, K)$ is populated. The projected many-body Hamiltonian simplifies to

$$H_\beta^{0 < \nu < 1} = P_\beta (H_0 + H_{\text{int}}) P_\beta, \quad (3)$$

where P_β projects onto the flavor β . The first term corresponds to the dispersion of the non-interaction band, and the projected Coulomb interaction corresponds to intra-flavor scattering. Case (ii): At $\nu_{\text{total}} = 3 + \nu$ with maximal inter-flavor interaction, we consider three fully filled flavors $(\bar{\sigma}, K)$, (σ, K') , $(\bar{\sigma}, K')$ as a background. The interaction between the three filled flavors and the remaining $\beta = (\sigma, K)$ flavor is given by a mean-field Hamiltonian

$$H_\beta^{MF} = \frac{1}{2A} \sum_{\beta' \neq \beta} \sum_{\mathbf{k}, \mathbf{k}', \mathbf{G}} \hat{n}_{\beta, \mathbf{k}} \langle \hat{n}_{\beta', \mathbf{k}'} \rangle \times (V_{\beta, \beta', \beta', \beta}(\mathbf{k}, \mathbf{k}', \mathbf{G}) + V_{\beta', \beta, \beta, \beta'}(\mathbf{k}', \mathbf{k}, \mathbf{G})), \quad (4)$$

where \mathbf{G} is reciprocal lattice vector, $\hat{n}_{\beta, \mathbf{k}} = \psi_{\beta, \mathbf{k}}^\dagger \psi_{\beta, \mathbf{k}}$, and $\langle \hat{n}_{\beta', \mathbf{k}'} \rangle = 1$ for the three background β' flavors. Note that here only the Hartree term is present since form factors of the Fock term between different flavors vanish. Then the full Hamiltonian reads

$$H_\beta^{\nu_{\text{total}}=3+\nu} = P_\beta (H_0 + H_\beta^{MF} + H_{\text{int}}) P_\beta. \quad (5)$$

Here $H_0 + H_\beta^{MF}$ represents the mean-field renormalized kinetic energy; see the red curve in Fig. 1 (a). The single-particle band width is significantly reduced from ~ 20 meV

to ~ 15 meV and may potentially stabilize correlated Hall states over a broader parameter range. For intermediate fillings $1 < \nu_{\text{total}} < 3$, similar but weaker Hartree effects occur, so we focus on the two extremal regimes above.

To investigate correlated Hall states, we perform exact diagonalization which handles intra-flavor scattering in Eqs. (3) and (5) exactly. The momentum grid is discretized as $\mathbf{k} = k_1 \mathbf{T}_1 + k_2 \mathbf{T}_2$, where $\mathbf{T}_{1(2)}$ are unit momentum vectors, $k_{1(2)} = 0, 1, 2, \dots, N_{1(2)} - 1$ labels the coordinate, and $N_s = N_1 N_2$ labels system size [46]. For filling fraction $\nu = N_p/N_s$ with N_p filled electron, the total momentum of occupied electrons $\mathbf{k} = \sum_{i=1}^{N_p} \mathbf{k}_i$ is a good quantum number, and the 2D coordinate (k_1, k_2) is mapped to the quasi-1d index $k_1 + N_1 k_2$ for convenience. In the following, we analyze gapped Hall states focusing on flavor polarization $\nu_{\text{total}} = 3 + \nu$.

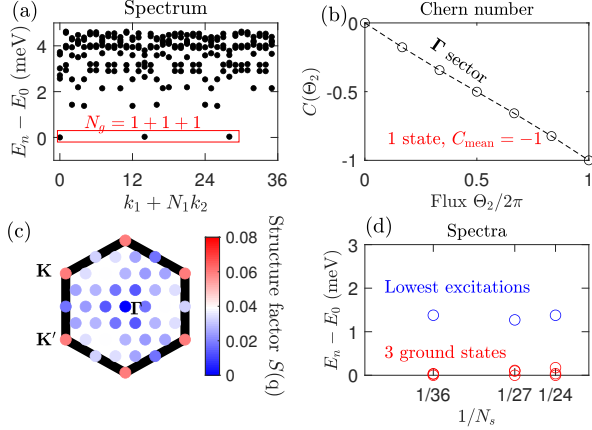


FIG. 2. **Quantum Hall crystal at $\nu_{\text{total}} = 3 + 2/3$ with $w_{AA}/w_{AB} = 0.6$.** (a) Many-body energy spectrum, (b) many-body Chern number, and (c) static structure factor $S(\mathbf{q})$ for $N_s = 36$. (d) Degeneracy and spectrum gap across different cluster sizes.

Quantum Hall crystal at $\nu_{\text{total}} = 3 + 2/3$. We first present evidence of the Hall crystal state at band filling $2/3$, as shown for an $N_s = 36$ cluster in Fig. 2 (a)-(c). We observe an interaction-induced many-body spectral gap in Fig. 2 (a) with $N_g = 1 + 1 + 1 = 3$ fold ground state degeneracy. The ground states reside in three momentum sectors Γ, K, K' independent of the cluster geometry. These ground state momenta are different from the FCIs [7]. To understand the topological property of this state, we compute the many-body Chern number [47–49] which connects to the Hall transport through $\sigma_H = \frac{e^2}{h} C_{\text{mean}}$ with $C_{\text{mean}} = \sum_{i=1}^{N_g} C_i/N_g$. Here the Chern number for a single many-body ground state $|\Phi_i\rangle$ is defined as an integral over twisted boundary conditions (θ_1, θ_2) :

$$C_i = C_i(2\pi) - C_i(0),$$

$$C_i(\Theta_2) = \frac{1}{2\pi} \int_0^{\Theta_2} d\theta_2 \int_0^{2\pi} d\theta_1 F_i(\theta_1, \theta_2), \quad (6)$$

where the many-body Berry curvature takes the form $F_i(\theta_1, \theta_2) = i(\langle \partial_{\theta_1} \Phi_i | \partial_{\theta_2} \Phi_i \rangle - \langle \partial_{\theta_2} \Phi_i | \partial_{\theta_1} \Phi_i \rangle)$. The Chern number $C_{\text{mean}} = -1$ for a representative momentum sector

can be read from Fig. 2 (b), where the minus sign is inherited from the band Chern number. Unlike FCIs, the violation of $C_{\text{mean}} = \nu C_{\text{band}}$ here further signals a non-FCI phase. We then compute the average static density-density structure factor

$$S(\mathbf{q}) = \frac{1}{N_s} [\langle \tilde{\rho}_{\mathbf{q}} \tilde{\rho}_{-\mathbf{q}} \rangle - \delta_{\mathbf{q},0} \langle \tilde{\rho}_{\mathbf{q}} \rangle \langle \tilde{\rho}_{-\mathbf{q}} \rangle], \quad (7)$$

where $\tilde{\rho}_{\mathbf{q}} \approx \sum_{\mathbf{k} \in \text{FBZ}} \langle \mathbf{k} | e^{-i\mathbf{q} \cdot \mathbf{r}} | \mathbf{k} + \mathbf{q} \rangle \psi_{\mathbf{k}}^\dagger \psi_{\mathbf{k}+\mathbf{q}}$ is the projected density operator. The $S(\mathbf{q})$ in Fig. 2 (c) exhibits sharp peaks at the K, K' points, signaling a CDW order with $\sqrt{3} \times \sqrt{3}$ enlarged unit-cell. In the SM, we further corroborate this structural reorganization through the real-space pair correlation function. Together, the spectrum degeneracy, integer Chern number, and CDW order conclusively establish a $\nu = 2/3$ QHC phase [14–18, 23–25]. Moreover, spectra obtained from various cluster sizes in Fig. 2 (d) imply that the phase remains gapped with fixed degeneracy in the thermodynamic limit. We also note that a similar crystal phase was recently predicted in twisted double bilayer graphene which also hosts high Chern bands [50]. These consistent observations suggest that the formation of this $\nu = 2/3$ phase may be a distinct characteristic of the $|C_{\text{band}}| = 2$ band.

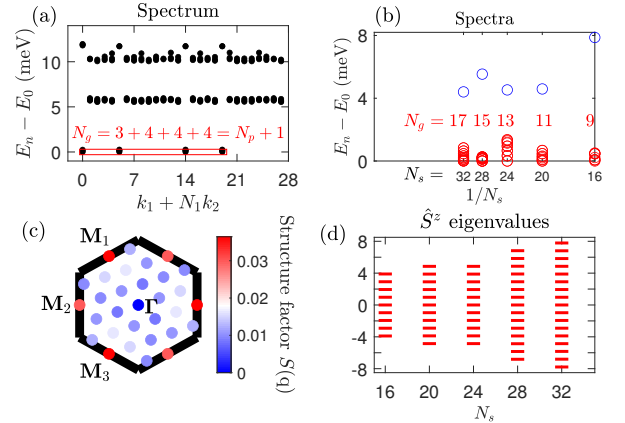


FIG. 3. **Quantum Hall ferromagnet at $\nu_{\text{total}} = 3 + 1/2$ with $w_{AA}/w_{AB} = 0.6$.** (a) Many-body energy spectrum on the $N_s = 28$ cluster. (b) Degeneracy and spectrum gap across different cluster sizes. (c) Static density-density structure factor $S(\mathbf{q})$ on the $N_s = 28$ cluster. (d) Emergent S^z quantum numbers for the pseudospin ferromagnetism with $S^z \approx -N_p/2, -N_p/2 + 1, \dots, N_p/2 - 1, N_p/2$.

Quantum Hall ferromagnet at $\nu_{\text{total}} = 3 + 1/2$. At half filling, we uncover a distinct gapped phase characterized by an extensive ground state degeneracy, contrasting sharply with the fixed degeneracies of QHCs or FCIs. For instance, on the $N_s = 28$ cluster, we observe $N_g = 3 + 4 + 4 + 4$ quasi-degenerate states in the four momentum sectors $\Gamma, M_1 = G_2/2, M_2 = G_1/2$ and $M_3 = (G_1 + G_2)/2$ [Fig. 3 (a)]. The spectra from different clusters in Fig. 3 (b) show an $N_g = N_p + 1$ fold degeneracy that scales with the system size, with an energy splitting much smaller than the bandwidth. This unusual degeneracy points towards a QHF state [39, 40, 51],

of which the extensive degeneracy arises from an emergent pseudospin SU(2) symmetry.

Reference 40 shows that an ideal $|C_{band}| = 2$ Chern band can be mapped to a spinful $|C_{band}| = 1$ band. In this framework, pseudospin ferromagnetism yields an $N_g = 2S + 1 = N_p + 1$ fold degeneracy, a quantized many-body Chern number $|C_{mean}| = 1$ and real-space CDW orders. However, it is unclear if such a state can emerge when the energy band becomes dispersive and is subjected to realistic Coulomb interactions. The average Chern number for each ground state is indeed $C_{mean} = -1$, in accordance with the picture that only a single component of the spinful system is occupied. The static structure factor with sharp Γ point peaks in Fig. 3 (c) indicates CDW order with 2×2 enlarged unit-cell *on average*. Unlike conventional CDW orders, the ordering wavevector \mathbf{Q} is non-unique and is related to the pseudospin polarization axis. The relation becomes clear by inspecting the pseudospin operator $\hat{S}^{x/y/z} = \sum_{\mathbf{k}} \hat{s}_{\mathbf{k}}^{x/y/z}$ through Brillouin zone folding [40]:

$$\hat{s}_{\mathbf{k}}^{x/y/z} = \tilde{\phi}_{\mathbf{k}}^\dagger \sigma^{x/y/z} \tilde{\phi}_{\mathbf{k}}/2, \quad \tilde{\phi}_{\mathbf{k}}^\dagger = [\tilde{\phi}_{0,\mathbf{k}}^\dagger, \tilde{\phi}_{1,\mathbf{k}}^\dagger] \quad (8)$$

where $\tilde{\phi}_{0,\mathbf{k}}^\dagger = \alpha_{\mathbf{k}} \psi_{\mathbf{k}}^\dagger + \beta_{\mathbf{k}} \psi_{\mathbf{k}+\frac{\mathbf{G}_2}{2}}^\dagger$ and $\tilde{\phi}_{1,\mathbf{k}}^\dagger = \alpha_{\mathbf{k}+\frac{\mathbf{G}_2}{2}} \psi_{\mathbf{k}+\frac{\mathbf{G}_2}{2}}^\dagger - \beta_{\mathbf{k}+\frac{\mathbf{G}_2}{2}} \psi_{\mathbf{k}+\frac{\mathbf{G}_1}{2}+\frac{\mathbf{G}_2}{2}}^\dagger$ are the single particle modes to be determined. A general ferromagnetic state is constructed as $\Phi(\varphi, \phi) = \prod_{\mathbf{k}} (\cos \frac{\varphi}{2} \tilde{\phi}_{0,\mathbf{k}}^\dagger + \sin \frac{\varphi}{2} e^{i\phi} \tilde{\phi}_{1,\mathbf{k}}^\dagger)$, and one can see that the CDW ordering wavevector \mathbf{Q} is locked to the ferromagnetism axis on the Bloch sphere. In SM, we show how to extract $(\alpha_{\mathbf{k}}, \beta_{\mathbf{k}})$ orbitals numerically via constructing CDW ordered states as north/south poles on the Bloch sphere. The spectrum of the $N_g \times N_g$ operator \hat{S}^z is shown in Fig. 3 (d), where the nearly quantized eigenvalues demonstrate that N_g -fold ground states indeed form a spin $S = N_s/4 = N_p/2$ multiplet. The quasi-degenerate ground states and the nearly quantized S^z quantum numbers suggest that the QHF states can exist in non-ideal band away from the chiral limit, in which the emergent SU(2) symmetry holds approximately.

Fractional Chern insulator at $\nu_{total} = 3 + \frac{1}{3}$. Remarkably, a translation-invariant FCI emerges at $\nu = 1/3$ —indicating dramatic particle-hole asymmetry for correlated states in this higher Chern band system. The energy spectrum in Fig. 4 (a) shows three-fold gapped ground states with momentum counting different from the QHC in Fig. 2 (a). The total Chern number $\sum C_i = -2$ for the three degenerate ground states [Fig. 4 (b)] yields a fractional Hall conductance $|\sigma_H| = 2e^2/3h$. Moreover, the absence of sharp structure factor peaks [Fig. 4 (c)] demonstrates that the real space moiré translation symmetry remains unbroken. Finite-size scaling [Fig. 4(d)] demonstrates a robust spectral gap and fixed degeneracy, signaling stability in the thermodynamic limit. To further characterize the topological order, we analyze the particle entanglement spectrum (PES), which encodes quasihole statistics [7, 52, 53]. The PES fingerprint (see SM) matches the Halperin (112) state [40, 54–56], a two-component pseudospin singlet quantum Hall state. This identification aligns

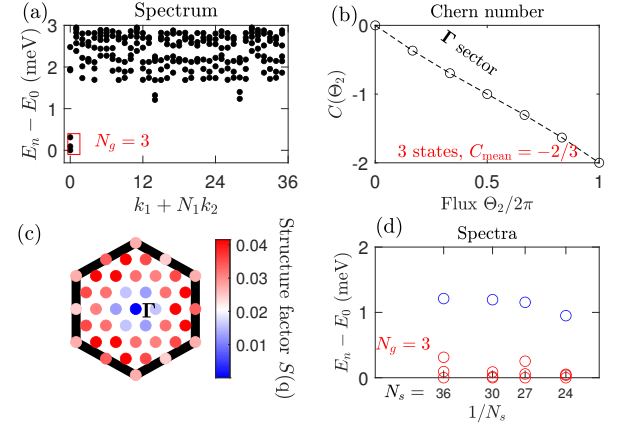


FIG. 4. **Fractional Chern insulator at $\nu_{total} = 3 + 1/3$ with $w_{AA}/w_{AB} = 0.6$.** (a) Many-body energy spectrum, (b) many-body Chern number, and (c) static structure factor $S(\mathbf{q})$ for $N_s = 36$. (d) Degeneracy and spectrum gap across different cluster sizes.

with the Chern-number decomposition $C_{band} = (-1) + (-1)$, analogous to spinful Landau levels. The emergence of multi-component FCI state in the higher Chern band opens pathways to engineer non-Abelian anyons via coupling to superconductors [57], offering a tantalizing platform for topological quantum computation.

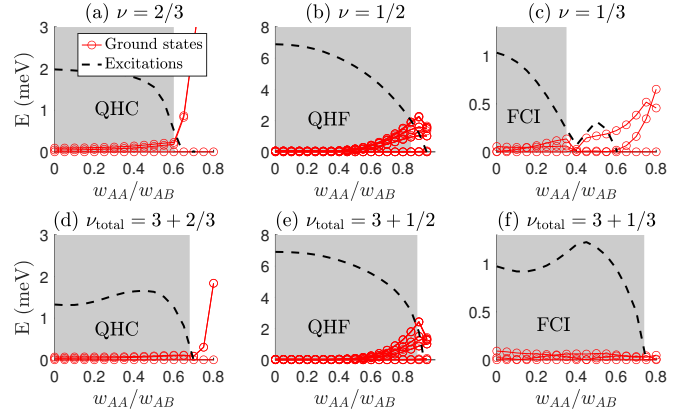


FIG. 5. **Energy spectra and quantitative phase diagrams versus w_{AA}/w_{AB} .** Shaded regions show ranges of gapped ground states. Red curves show the evolution of N_g quasi-degenerate ground states, while the black curves show the lowest excitation energies. System sizes for simulating the three phases are $N_s = 27, 28, 24$, on which the degeneracies are $N_g = 3, 15, 3$, respectively.

Global phase diagram. Having identified the three gapped anomalous Hall states, we examine their stability across the full range of lattice corrugation parametrized through w_{AA}/w_{AB} . The essential control parameter is the interaction-to-bandwidth ratio U/W , since Coulomb-driven gaps can only open if U/W is sufficient large. Panels (a-c) of Fig. 5 show that, for the low filling regime $0 < \nu < 1$, all three phases are stabilized close to the chiral limit $w_{AA} = 0$, where the single-particle bandwidth is minimal and U/W is maxi-

mal. The critical threshold for the FCI state at $\nu = 1/3$ is about $w_{AA} \approx 0.35w_{AB}$, much lower than the expected realistic value. By contrast, in the high-filling regime $\nu_{\text{total}} = 3 + \nu$, interband interaction renormalizes the dispersion and thereby boosts U/W . As panels (d-f) demonstrate, this enhanced interaction strength stabilizes all three phases over a much wider corrugation window. In particular, the parameter range of the FCI at $\nu_{\text{total}} = 3 + 1/3$ is significantly extended compared to its $\nu = 1/3$ counterpart. The overall phase diagrams suggest that the FCI state is relatively more fragile than the other two states, while the QHF phase exhibits the largest gap and widest stability window, suggesting it is the most accessible for observation.

In summary, our work predicts a series of novel gapped Hall states at fractional filling of HTG subjected to a substrate potential. The phase diagram reveals three distinct phases in realistic higher Chern bands beyond the chiral limit: a quantum Hall crystal, a quantum Hall ferromagnet, and a Halperin-type fractional Chern insulator. Each phase exhibits either unique symmetry-breaking orders or topological orders compared to those expected in the $|C_{\text{band}}| = 1$ band, and they can be differentiated by their Hall conductance or CDW ordering pattern in real- and momentum-space. Moreover, the filling fractions $\nu = 2/3, 7/2$ reported in the recent transport experiment partially align with our predicted doping sequence. Future transport measurements at low temperature at optimal carrier densities $\nu_{\text{total}} = 3 + \nu$ regime may further clarify the nature of the quantum states observed in experiments.

Acknowledgment. This work is supported by the US National Science Foundation (NSF) Grant No. PHY-2216774. Additional support was provided by the Caltech Institute for Quantum Information and Matter, an NSF Physics Frontiers Center (NSF Grant PHY-2317110).

* sen.niu@csun.edu

† alicej@caltech.edu

‡ donna.sheng@csun.edu

§ yang.peng@csun.edu

- [1] E. Y. Andrei, D. K. Efetov, P. Jarillo-Herrero, A. H. MacDonald, K. F. Mak, T. Senthil, E. Tutuc, A. Yazdani, and A. F. Young, The marvels of moiré materials, *Nature Reviews Materials* **6**, 201 (2021).
- [2] K. F. Mak and J. Shan, Semiconductor moiré materials, *Nature Nanotechnology* **17**, 686 (2022).
- [3] E. Tang, J.-W. Mei, and X.-G. Wen, High-temperature fractional quantum hall states, *Physical review letters* **106**, 236802 (2011).
- [4] K. Sun, Z. Gu, H. Katsura, and S. Das Sarma, Nearly flatbands with nontrivial topology, *Physical review letters* **106**, 236803 (2011).
- [5] T. Neupert, L. Santos, C. Chamon, and C. Mudry, Fractional quantum hall states at zero magnetic field, *Physical review letters* **106**, 236804 (2011).
- [6] D. Sheng, Z.-C. Gu, K. Sun, and L. Sheng, Fractional quantum hall effect in the absence of landau levels, *Nature communications* **2**, 389 (2011).

- [7] N. Regnault and B. A. Bernevig, Fractional chern insulator, *Physical Review X* **1**, 021014 (2011).
- [8] J. Cai, E. Anderson, C. Wang, X. Zhang, X. Liu, W. Holtzmann, Y. Zhang, F. Fan, T. Taniguchi, K. Watanabe, *et al.*, Signatures of fractional quantum anomalous hall states in twisted mote2, *Nature* **622**, 63 (2023).
- [9] Y. Zeng, Z. Xia, K. Kang, J. Zhu, P. Knüppel, C. Vaswani, K. Watanabe, T. Taniguchi, K. F. Mak, and J. Shan, Thermodynamic evidence of fractional chern insulator in moiré mote2, *Nature* **622**, 69 (2023).
- [10] H. Park, J. Cai, E. Anderson, Y. Zhang, J. Zhu, X. Liu, C. Wang, W. Holtzmann, C. Hu, Z. Liu, *et al.*, Observation of fractionally quantized anomalous hall effect, *Nature* **622**, 74 (2023).
- [11] F. Xu, Z. Sun, T. Jia, C. Liu, C. Xu, C. Li, Y. Gu, K. Watanabe, T. Taniguchi, B. Tong, *et al.*, Observation of integer and fractional quantum anomalous hall effects in twisted bilayer mote 2, *Physical Review X* **13**, 031037 (2023).
- [12] Z. Lu, T. Han, Y. Yao, A. P. Reddy, J. Yang, J. Seo, K. Watanabe, T. Taniguchi, L. Fu, and L. Ju, Fractional quantum anomalous hall effect in multilayer graphene, *Nature* **626**, 759 (2024).
- [13] Z. Tešanović, F. Axel, and B. Halperin, “hall crystal” versus wigner crystal, *Physical Review B* **39**, 8525 (1989).
- [14] H. Pan, M. Xie, F. Wu, and S. Das Sarma, Topological phases in ab-stacked mote 2/wse 2: Z 2 topological insulators, chern insulators, and topological charge density waves, *Physical Review Letters* **129**, 056804 (2022).
- [15] C. Xu, J. Li, Y. Xu, Z. Bi, and Y. Zhang, Maximally localized wannier functions, interaction models, and fractional quantum anomalous hall effect in twisted bilayer mote2, *Proceedings of the National Academy of Sciences* **121**, e2316749121 (2024).
- [16] X.-Y. Song, C.-M. Jian, L. Fu, and C. Xu, Intertwined fractional quantum anomalous hall states and charge density waves, *Physical Review B* **109**, 115116 (2024).
- [17] D. Sheng, A. P. Reddy, A. Abouelkomsan, E. J. Bergholtz, and L. Fu, Quantum anomalous hall crystal at fractional filling of moiré superlattices, *Physical Review Letters* **133**, 066601 (2024).
- [18] J. Dong, T. Wang, T. Wang, T. Soejima, M. P. Zaletel, A. Vishwanath, and D. E. Parker, Anomalous hall crystals in rhombohedral multilayer graphene. i. interaction-driven chern bands and fractional quantum hall states at zero magnetic field, *Physical Review Letters* **133**, 206503 (2024).
- [19] Z. Dong, A. S. Patri, and T. Senthil, Stability of anomalous hall crystals in multilayer rhombohedral graphene, *Physical Review B* **110**, 205130 (2024).
- [20] T. Soejima, J. Dong, T. Wang, T. Wang, M. P. Zaletel, A. Vishwanath, and D. E. Parker, Anomalous hall crystals in rhombohedral multilayer graphene. ii. general mechanism and a minimal model, *Physical Review B* **110**, 205124 (2024).
- [21] T. Tan and T. Devakul, Parent berry curvature and the ideal anomalous hall crystal, *Physical Review X* **14**, 041040 (2024).
- [22] N. Paul, G. Shavit, and L. Fu, Designing (higher) hall crystals, *arXiv preprint arXiv:2410.03888* (2024).
- [23] H. Polshyn, Y. Zhang, M. A. Kumar, T. Soejima, P. Ledwith, K. Watanabe, T. Taniguchi, A. Vishwanath, M. P. Zaletel, and A. F. Young, Topological charge density waves at half-integer filling of a moiré superlattice, *Nature Physics* **18**, 42 (2022).
- [24] D. Waters, A. Okounkova, R. Su, B. Zhou, J. Yao, K. Watanabe, T. Taniguchi, X. Xu, Y.-H. Zhang, J. Folk, *et al.*, Chern insulators at integer and fractional filling in moiré pentalayer graphene, *Physical Review X* **15**, 011045 (2025).
- [25] Z. Lu, T. Han, Y. Yao, Z. Hadjri, J. Yang, J. Seo, L. Shi, S. Ye, K. Watanabe, T. Taniguchi, *et al.*, Extended quantum anomalous hall states in graphene/hbn moiré superlattices, *Nature* , 1

- (2025).
- [26] R. Su, D. Waters, B. Zhou, K. Watanabe, T. Taniguchi, Y.-H. Zhang, M. Yankowitz, and J. Folk, Moiré-driven topological electronic crystals in twisted graphene, *Nature*, 1 (2025).
 - [27] J. C. Hoke, Y. Li, Y. Hu, J. May-Mann, K. Watanabe, T. Taniguchi, T. Devakul, and B. E. Feldman, Imaging supermoire relaxation and conductive domain walls in helical trilayer graphene, *arXiv preprint arXiv:2410.16269* (2024).
 - [28] N. Nakatsuji, T. Kawakami, and M. Koshino, Multiscale lattice relaxation in general twisted trilayer graphenes, *Physical Review X* **13**, 041007 (2023).
 - [29] T. Devakul, P. J. Ledwith, L.-Q. Xia, A. Uri, S. C. de la Barrera, P. Jarillo-Herrero, and L. Fu, Magic-angle helical trilayer graphene, *Science Advances* **9**, eadi6063 (2023).
 - [30] D. Guerci, Y. Mao, and C. Mora, Chern mosaic and ideal flat bands in equal-twist trilayer graphene, *Physical Review Research* **6**, L022025 (2024).
 - [31] D. Guerci, Y. Mao, and C. Mora, Nature of even and odd magic angles in helical twisted trilayer graphene, *Physical Review B* **109**, 205411 (2024).
 - [32] C. Yang, J. May-Mann, Z. Zhu, and T. Devakul, Multi-moiré trilayer graphene: lattice relaxation, electronic structure, and magic angles, *Physical Review B* **110**, 115434 (2024).
 - [33] L.-Q. Xia, S. C. de la Barrera, A. Uri, A. Sharpe, Y. H. Kwan, Z. Zhu, K. Watanabe, T. Taniguchi, D. Goldhaber-Gordon, L. Fu, *et al.*, Topological bands and correlated states in helical trilayer graphene, *Nature Physics*, 1 (2025).
 - [34] Y. H. Kwan, P. J. Ledwith, C. F. B. Lo, and T. Devakul, Strong-coupling topological states and phase transitions in helical trilayer graphene, *Physical Review B* **109**, 125141 (2024).
 - [35] Y. H. Kwan, T. Tan, and T. Devakul, Fractional chern mosaic in supermoiré graphene, *arXiv preprint arXiv:2411.08880* (2024).
 - [36] M. Barkeshli and X.-L. Qi, Topological nematic states and non-abelian lattice dislocations, *Physical Review X* **2**, 031013 (2012).
 - [37] Y.-L. Wu, N. Regnault, and B. A. Bernevig, Haldane statistics for fractional chern insulators with an arbitrary chern number, *Physical Review B* **89**, 155113 (2014).
 - [38] Z. Liu, A. Abouelkomsan, and E. J. Bergholtz, Gate-tunable fractional chern insulators in twisted double bilayer graphene, *Physical Review Letters* **126**, 026801 (2021).
 - [39] P. Wilhelm, T. Lang, M. S. Scheurer, and A. Läuchli, Non-coplanar magnetism, topological density wave order and emergent symmetry at half-integer filling of moiré chern bands, *SciPost Physics* **14**, 040 (2023).
 - [40] J. Dong, P. J. Ledwith, E. Khalaf, J. Y. Lee, and A. Vishwanath, Many-body ground states from decomposition of ideal higher chern bands: Applications to chirally twisted graphene multilayers, *Physical Review Research* **5**, 023166 (2023).
 - [41] G. Giovannetti, P. A. Khomyakov, G. Brocks, P. J. Kelly, and J. Van Den Brink, Substrate-induced band gap in graphene on hexagonal boron nitride: Ab initio density functional calculations, *Physical Review B—Condensed Matter and Materials Physics* **76**, 073103 (2007).
 - [42] A. P. Reddy, F. Alsallom, Y. Zhang, T. Devakul, and L. Fu, Fractional quantum anomalous hall states in twisted bilayer mote2 and wse2, *Physical Review B* **108**, 085117 (2023).
 - [43] Y. Cao, V. Fatemi, S. Fang, K. Watanabe, T. Taniguchi, E. Kaxiras, and P. Jarillo-Herrero, Magic-angle graphene superlattices: a new platform for unconventional superconductivity, *arXiv preprint arXiv:1803.02342* (2018).
 - [44] U. Zondiner, A. Rozen, D. Rodan-Legrain, Y. Cao, R. Queiroz, T. Taniguchi, K. Watanabe, Y. Oreg, F. von Oppen, A. Stern, *et al.*, Cascade of phase transitions and dirac revivals in magic-angle graphene, *Nature* **582**, 203 (2020).
 - [45] D. Wong, K. P. Nuckolls, M. Oh, B. Lian, Y. Xie, S. Jeon, K. Watanabe, T. Taniguchi, B. A. Bernevig, and A. Yazdani, Cascade of electronic transitions in magic-angle twisted bilayer graphene, *Nature* **582**, 198 (2020).
 - [46] In Supplemental Materials (SM), we provide extra information for band structures, finite-sized clusters used in exact diagonalization, pair correlation functions and further numerical evidences supporting QHF and FCI states..
 - [47] Q. Niu, D. J. Thouless, and Y.-S. Wu, Quantized hall conductance as a topological invariant, *Physical Review B* **31**, 3372 (1985).
 - [48] D. N. Sheng, X. Wan, E. H. Rezayi, K. Yang, R. N. Bhatt, and F. D. M. Haldane, Disorder-driven collapse of the mobility gap and transition to an insulator in the fractional quantum hall effect, *Phys. Rev. Lett.* **90**, 256802 (2003).
 - [49] T. Fukui, Y. Hatsugai, and H. Suzuki, Chern numbers in discretized brillouin zone: efficient method of computing (spin) hall conductances, *Journal of the Physical Society of Japan* **74**, 1674 (2005).
 - [50] R. Perea-Causin, H. Liu, and E. J. Bergholtz, Quantum anomalous hall crystals in moiré bands with higher chern number, *arXiv preprint arXiv:2412.02745* (2024).
 - [51] Z. F. Ezawa and G. Tsitsishvili, Quantum hall ferromagnets, *Reports on Progress in Physics* **72**, 086502 (2009).
 - [52] H. Li and F. D. M. Haldane, Entanglement spectrum as a generalization of entanglement entropy: Identification of topological order in non-abelian fractional quantum hall effect states, *Physical review letters* **101**, 010504 (2008).
 - [53] A. Sterdyniak, N. Regnault, and B. A. Bernevig, Extracting excitations from model state entanglement, *Physical review letters* **106**, 100405 (2011).
 - [54] B. I. Halperin, Theory of the quantized hall conductance, *helv. phys. acta* **56**, 75 (1983).
 - [55] S. Geraedts, M. P. Zaletel, Z. Papić, and R. S. Mong, Competing abelian and non-abelian topological orders in $\nu = 1/3 + 1/3$ quantum hall bilayers, *Physical Review B* **91**, 205139 (2015).
 - [56] Y. Liu and Z. Zhu, Engineering fractional chern insulators through periodic strain in monolayer graphene and transition metal dichalcogenides, *arXiv preprint arXiv:2407.12411* (2024).
 - [57] R. S. Mong, D. J. Clarke, J. Alicea, N. H. Lindner, P. Fendley, C. Nayak, Y. Oreg, A. Stern, E. Berg, K. Shtengel, *et al.*, Universal topological quantum computation from a superconductor-abelian quantum hall heterostructure, *Physical Review X* **4**, 011036 (2014).

Supplemental materials

I. EFFECTS OF w_{AA} AND SUBSTRATE POTENTIAL ON BAND STRUCTURES

It is known that in the chiral limit [S1] and at the magic angle $\theta = 1.5^\circ$, the two central Chern bands with $C_{band} = +1, -2$ have exact zero energies at the K valley. As the two bands are eigenstates of the sublattice basis, a uniform substrate potential $\mu_1 = (-8, -8, -8)$ meV can separate the two bands perfectly without changing the dispersion; see Fig. S1 (a). Due to the sign of the potential, the $C_{band} = -2$ band has positive energy and the $C_{band} = +1$ band has negative energy. However, such uniform potential is not realistic in real materials. Figure S1 (b)-(d) explores different types of non-uniform substrate potentials including a single-layer potential $\mu_2 = (0, 0, -20)$ meV, a potential acting on both top and bottom layers $\mu_3 = (-8, 0, -8)$ meV, and a potential decaying from the bottom layer to the top layer $\mu_4 = (-4, -6, -8)$ meV. One can see that the two bands separate most effectively for μ_3 and μ_4 ; we stick to μ_4 throughout this work but expect μ_3 (and possibly also μ_2) to exhibit similar phenomenology. Figure S1 (e) further considers realistic corrugation $w_{AA} = 0.6w_{AB}$ which is far away from the chiral limit, yielding a more dispersive band with a bandwidth close to 20 meV. In Fig. S1 (f), one can see that at a slightly different twist angle $\theta = 1.44^\circ$ used in main text, the band structures are similar. In the opposite valley K' , the signs of Chern numbers reverse, i.e., the upper band has $C_{band} = +2$ and the lower band has $C_{band} = -1$.

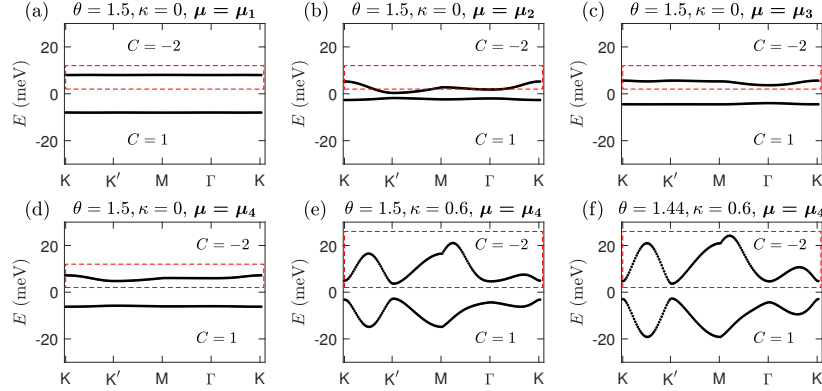


FIG. S1. Non-interacting Chern bands for different $\theta, \kappa = w_{AA}/w_{AB}$ and substrate potential μ . Here $\mu_1 = (-8, -8, -8)$ meV corresponds to a uniform potential, $\mu_2 = (0, 0, -20)$ meV is a single-layer potential, $\mu_3 = (-8, 0, -8)$ meV is a potential acting on both bottom and top layers, and $\mu_4 = (-4, -6, -8)$ meV is a potential that decays from bottom layer to top layer which is used in the main text.

II. FINITE CLUSTERS FOR EXACT DIAGONALIZATION

We denote $\mathbf{a}_1, \mathbf{a}_2$ as the lattice vectors of the moiré triangular superlattice. The reciprocal lattice vectors takes the form

$$\mathbf{g}_i = \frac{2\pi\epsilon_{ij}\mathbf{a}_j \times \hat{z}}{|\mathbf{a}_1 \times \mathbf{a}_2|}. \quad (\text{S1})$$

A finite cluster can be determined from real space translation vectors $\mathbf{L}_1 = m_1\mathbf{a}_1 + n_1\mathbf{a}_2$, $\mathbf{L}_2 = m_2\mathbf{a}_1 + n_2\mathbf{a}_2$, where vectors $\mathbf{L}_1, \mathbf{L}_2$ define the translation invariance of the finite cluster on an infinite lattice. The allowed plane-wave momenta take the form

$$\mathbf{T}_i = \frac{2\pi\epsilon_{ij}\mathbf{L}_j \times \hat{z}}{|\mathbf{L}_1 \times \mathbf{L}_2|}, \quad (\text{S2})$$

which satisfies $\mathbf{L}_i \cdot \mathbf{T}_j = 2\pi\delta_{ij}$. The discrete momentum points take the form of integer combinations $\mathbf{k} = k_1\mathbf{T}_1 + k_2\mathbf{T}_2$, where $k_i = 0, 1, \dots, N_i - 1$ and $N_1N_2 = N_s$. In our many-body calculations, we use the total momentum of occupied

N_s	\mathbf{L}_1	\mathbf{L}_2	N_1	N_2	\mathbf{K}, \mathbf{K}' points
16	(4, 0)	(0, 4)	4	4	No
20	(2, 2)	(4, -6)	2	10	No
24	(4, -4)	(0, 6)	4	6	No
24	(1, 4)	(5, -4)	1	24	Yes
26	(0, 13)	(2, 4)	13	2	No
27	(6, -3)	(3, -6)	3	9	Yes
28	(-2, 6)	(4, 2)	2	14	No
30	(5, 0)	(0, 6)	5	6	No
32	(2, 4)	(6, -4)	2	16	No
36	(6, 0)	(0, 6)	6	6	Yes

TABLE SI. Information about finite clusters used in ED.

electrons $\mathbf{k} = \sum_{i=1}^{\nu N_s} \mathbf{k}_i$ as a symmetry to block diagonalize the many-body Hamiltonian. For each cluster the total number of \mathbf{k} sectors equals to the cluster size N_s .

In Table SI, we show information for all the clusters used in numerical calculations. Note that since the quantum Hall crystals at $\nu = 2/3$ have ground state momenta Γ, K, K' , numerical diagonalization on clusters without \mathbf{K}, \mathbf{K}' is biased. Therefore, among the two $N_s = 24$ clusters in the table, we take the one with $\mathbf{L}_1 = (1, 4)$, $\mathbf{L}_2 = (5, -4)$ for calculations at $\nu = 2/3$, and take the one with $\mathbf{L}_1 = (4, -4)$, $\mathbf{L}_2 = (0, 6)$ otherwise.

III. FURTHER NUMERICAL ANALYSIS FOR QUANTUM HALL FERROMAGNETS

In the main text, based on the observations of the extensive ground state degeneracy and the presence of \mathbf{M} point structure factor peaks, we propose that the half-filled ground states are quantum Hall ferromagnets. To further substantiate this proposition, we analyze the symmetry-breaking charge density wave (CDW) orders and identify signatures of emergent $SU(2)$ symmetry, including pseudospin ferromagnetism and suppressed ground state energy splitting.

A. Symmetry breaking orders in quantum Hall ferromagnets

As demonstrated in Ref. S2, ideal Chern bands permit the construction of many-body ground states resembling mean-field product states. For our non-ideal band under realistic Coulomb interactions, we quantify the deviation of a generic many-body state $\tilde{\Phi}$ from a product state using the momentum-space correlation matrix:

$$O_{i,j} = \langle \tilde{\Phi} | \psi_{\mathbf{k}_i}^\dagger \psi_{\mathbf{k}_j} | \tilde{\Phi} \rangle, \quad (\text{S3})$$

where $\psi_{\mathbf{k}_i}^\dagger$ creates a Bloch state at momentum \mathbf{k}_i . In product states, O has eigenvalues strictly 0 (unoccupied) or 1 (occupied), while interacting states exhibit eigenvalues distributed continuously between 0 and 1.

Figures S2 (a)–(d) display the eigenvalues of O for the N_g -fold degenerate momentum-resolved ground states $|\Phi_{\mathbf{k}}^i\rangle$, with total momentum $\mathbf{k} \in \{\Gamma, \mathbf{M}_1, \mathbf{M}_2, \mathbf{M}_3\}$ and i labeling states within each momentum sector. Momentum conservation restricts O to be diagonal, where the diagonal elements $\langle \hat{n}_{\mathbf{k}} \rangle \equiv \langle \psi_{\mathbf{k}}^\dagger \psi_{\mathbf{k}} \rangle$ represent the momentum distribution. The observed deviation of $\langle n_{\mathbf{k}} \rangle$ from 0 and 1 confirms that these states are strongly correlated and distinct from product states.

Inspired by mean-field analysis in Ref. S3, a general symmetry-broken state can be represented by linear superposition from distinct momentum sectors:

$$\tilde{\Phi} = \sum_i a_i |\Phi_{\Gamma}^i\rangle + \sum_j b_j |\Phi_{\mathbf{M}_1}^j\rangle + \sum_k c_k |\Phi_{\mathbf{M}_2}^k\rangle + \sum_l d_l |\Phi_{\mathbf{M}_3}^l\rangle, \quad (\text{S4})$$

where a_i, b_j, c_k, d_l are parameters to be determined. In the simplest scenario involving only two momentum sectors, we construct states with ordering wavevector $\mathbf{Q} \in \{\mathbf{M}_1, \mathbf{M}_2, \mathbf{M}_3\}$:

$$\tilde{\Phi}_{\mathbf{k}, \mathbf{k}+\mathbf{Q}} = \sum_i a_i |\Phi_{\mathbf{k}}^i\rangle + \sum_j b_j |\Phi_{\mathbf{k}+\mathbf{Q}}^j\rangle. \quad (\text{S5})$$

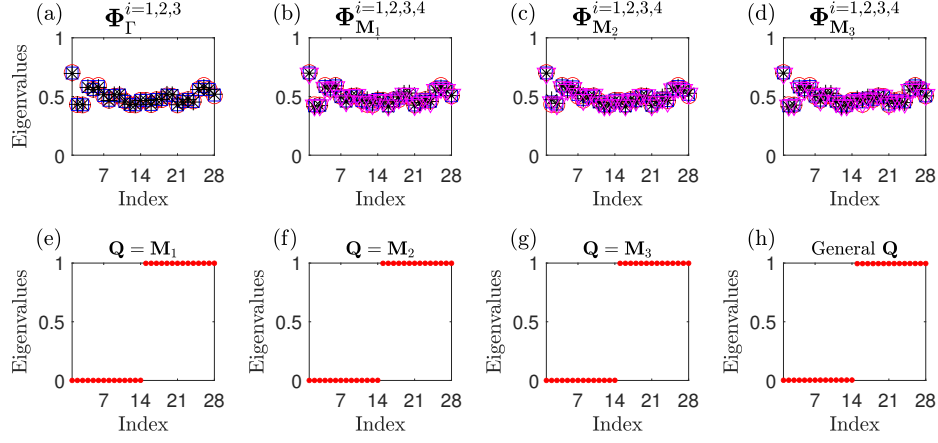


FIG. S2. Orbital occupation number revealed by eigenvalues of momentum space correlation matrix $\langle \psi_{k_1}^\dagger \psi_{k_2} \rangle$ with $\nu_{\text{total}} = 3 + 1/2$, $w_{AA} = 0.6w_{AB}$, $N_s = 28$. (a)-(d) show the results for the 3, 4, 4, 4-fold ground states on the four momentum sectors $\Gamma, \mathbf{M}_1, \mathbf{M}_2, \mathbf{M}_3$, respectively. Since the exact eigenstates are momentum conserving, the correlation matrices are diagonal and the elements simply correspond to Bloch momentum distribution $\langle \psi_{\mathbf{k}}^\dagger \psi_{\mathbf{k}} \rangle$. (e)-(g) show the results for mean-field like states obtained from linear combinations of states with different momenta using Eq. (S5). (h) shows a general linearly combined state using Eq. (S4). For (a)-(d) the indices $1, \dots, N_s$ label momentum, whereas in (e)-(h), the indices $1, \dots, N_s$ refer to the order of eigenvalues sorted in ascending order.

This superposition generates off-diagonal correlations between \mathbf{k}_i and $\mathbf{k}_i + \mathbf{Q}$, reducing the correlation matrix O to block-diagonal 2×2 form.

As shown in Figs. S2 (e)-(g), optimized coefficients a_i, b_j in Eq. (S5) yield correlation matrix eigenvalues approaching 0 or 1 for all choices of \mathbf{Q} , confirming proximity to mean-field product states. The eigenvectors of O define the (almost) fully occupied orbitals:

$$\phi_{\mathbf{k}}^\dagger = \alpha_{\mathbf{k}} \psi_{\mathbf{k}}^\dagger + \beta_{\mathbf{k}} \psi_{\mathbf{k}+\mathbf{Q}}^\dagger, \quad (\text{S6})$$

which will be utilized in subsequent analysis. For the general superposition in Eq. (S4), O reduces to 4×4 blocks while still admitting mean-field-like solutions [Fig. S2 (h)]. We now characterize the symmetry-breaking orders of these linearly combined states.

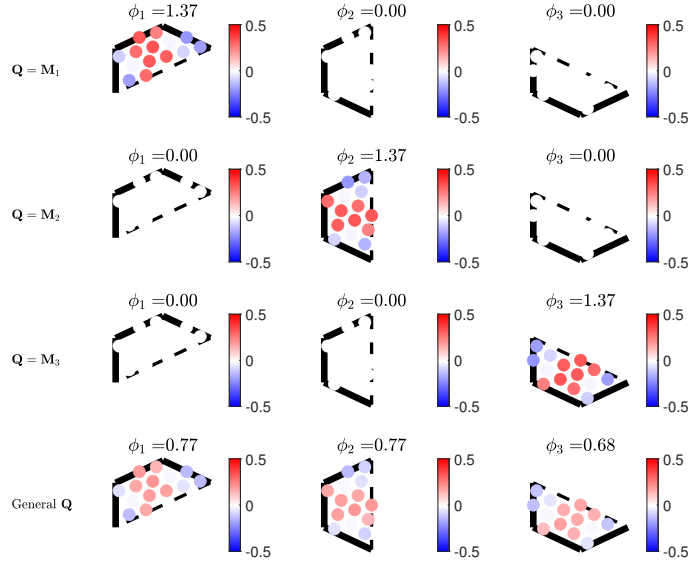


FIG. S3. Momentum space contributions to the charge density wave order parameter ϕ_i using Eq. (S7). Four different rows correspond to four different linearly combined mean-field-like states in Fig. S2(e)-(g). Three columns ϕ_1, ϕ_2, ϕ_3 correspond to three different ways of folding Brillouin zone on the triangular lattice.

To characterize CDW orders in the superposed many-body states, we compute order parameters following Refs. S2 and S3:

$$\phi_i = \frac{1}{2} \sum_{\mathbf{k} \in \text{folded BZ}} \sum_{\xi=\pm 1} F(\mathbf{k}, \xi \mathbf{M}_i) \langle \tilde{\Phi} | \psi_{\mathbf{k}}^\dagger \psi_{\mathbf{k}+\xi \mathbf{M}_i} | \tilde{\Phi} \rangle + h.c., \quad (\text{S7})$$

where $F(\mathbf{k}, \xi \mathbf{q}) = \langle \mathbf{k} | e^{-i\mathbf{q} \cdot \mathbf{r}} | \mathbf{k} + \mathbf{q} \rangle$ is the form factor between Bloch states and \mathbf{k} corresponds to the Bloch momentum in the folded Brillouin zone. Figure S3 displays ϕ_i and their folded Brillouin Zone distributions for the optimized states in Figs. S2 (e)-(h). When $\mathbf{Q} = \mathbf{M}_j$ (single- Q states), only ϕ_j is nonzero by construction. These correspond to pseudospin-polarized states along the x, y, z axes of an emergent Bloch sphere. For any solution $\{a_i, b_j\}$ in Eq. (S7), the sign-flipped coefficients $\{a_i, -b_j\}$ yield an order parameter with opposite sign. The resulting state pairs $|\pm Z\rangle$ (similarly $|\pm X\rangle, |\pm Y\rangle$) represent opposite pseudospin polarizations along the same axis. For example, if $\mathbf{Q} = \mathbf{M}_2$, these have order parameters $(0, \pm\phi_2, 0)$. Their correlation matrices share identical diagonal elements but opposite off-diagonal signs. Consequently, if $|+Z\rangle$ has (almost) fully occupied orbitals

$$\phi_{\mathbf{k}}^\dagger = \alpha_{\mathbf{k}} \psi_{\mathbf{k}}^\dagger + \beta_{\mathbf{k}} \psi_{\mathbf{k}+\mathbf{Q}}^\dagger, \quad (\text{S8})$$

then $|-Z\rangle$ has

$$\phi_{\mathbf{k}}^\dagger = \alpha_{\mathbf{k}} \psi_{\mathbf{k}}^\dagger - \beta_{\mathbf{k}} \psi_{\mathbf{k}+\mathbf{Q}}^\dagger. \quad (\text{S9})$$

For superpositions spanning all momentum sectors [Eq. (S4)], all $\phi_{1,2,3}$ components can be nonzero. By sampling randomized coefficients and then optimizing them, we obtain mean-field-like states whose order parameters (ϕ_1, ϕ_2, ϕ_3) trace a spherical manifold. However, this order parameter alone cannot confirm emergent SU(2) symmetry. In the following subsection, we analyze this through pseudospin operators derived from Brillouin zone folding.

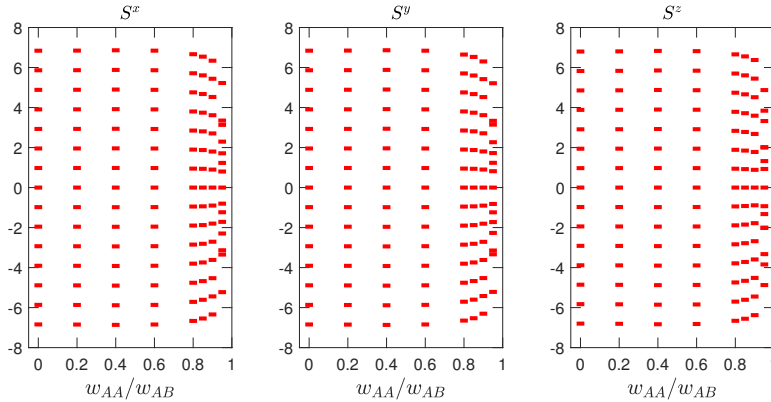


FIG. S4. $\hat{S}^{x/y/z}$ quantum numbers which are computed by diagonalizing the pseudo-spin $\hat{S}^{x/y/z}$ operators for $\nu_{\text{total}} = 3 + 1/2$ on the $N_s = 28$ cluster. The values are approximately $-N_p/2, -N_p/2 + 1, \dots, N_p/2 - 1, N_p/2$ for $w_{AA}/w_{AB} \leq 0.9$ before the spectrum gap vanishes.

B. Emergent SU(2) symmetry

The quasi-degenerate ground states and near-integer occupation spectra [Figs. S2 (e)-(h)] provide strong evidence for emergent SU(2) ferromagnetism in dispersive Chern bands. Motivated by these observations and the Brillouin zone folding framework in Ref. S2, we define pseudospin operators through the following construction:

$$\begin{aligned} \hat{S}^{x/y/z} &= \sum_{\mathbf{k} \in \text{folded BZ}} \hat{s}_{\mathbf{k}}^{x/y/z}, \\ \hat{s}_{\mathbf{k}}^x &= \frac{1}{2} \left(\tilde{\phi}_{0,\mathbf{k}}^\dagger \tilde{\phi}_{1,\mathbf{k}} + \tilde{\phi}_{1,\mathbf{k}}^\dagger \tilde{\phi}_{0,\mathbf{k}} \right), \\ \hat{s}_{\mathbf{k}}^y &= \frac{i}{2} \left(-\tilde{\phi}_{0,\mathbf{k}}^\dagger \tilde{\phi}_{1,\mathbf{k}} + \tilde{\phi}_{1,\mathbf{k}}^\dagger \tilde{\phi}_{0,\mathbf{k}} \right), \\ \hat{s}_{\mathbf{k}}^z &= \frac{1}{2} \left(\tilde{\phi}_{0,\mathbf{k}}^\dagger \tilde{\phi}_{0,\mathbf{k}} - \tilde{\phi}_{1,\mathbf{k}}^\dagger \tilde{\phi}_{1,\mathbf{k}} \right), \end{aligned} \quad (\text{S10})$$

where the momentum sum covers the folded Brillouin zone, and the orbital operators are defined as

$$\begin{aligned}\tilde{\phi}_{0,\mathbf{k}}^\dagger &= \alpha_{\mathbf{k}}\psi_{\mathbf{k}}^\dagger + \beta_{\mathbf{k}}\psi_{\mathbf{k}+\frac{\mathbf{G}_1}{2}}^\dagger, \\ \tilde{\phi}_{1,\mathbf{k}}^\dagger &= \alpha_{\mathbf{k}+\frac{\mathbf{G}_2}{2}}\psi_{\mathbf{k}+\frac{\mathbf{G}_2}{2}}^\dagger - \beta_{\mathbf{k}+\frac{\mathbf{G}_2}{2}}\psi_{\mathbf{k}+\frac{\mathbf{G}_1}{2}+\frac{\mathbf{G}_2}{2}}^\dagger.\end{aligned}\quad (\text{S11})$$

Here $\mathbf{G}_1/2 = \mathbf{M}_2$, $\mathbf{G}_2/2 = \mathbf{M}_1$, $\mathbf{G}_1/2 + \mathbf{G}_2/2 = \mathbf{M}_3$, and $\mathbf{G}_1, \mathbf{G}_2, \mathbf{G}_3$ form the reciprocal lattice basis of the triangular lattice. The coefficients $(\alpha_{\mathbf{k}}, \beta_{\mathbf{k}})$ are chosen to be the occupied orbitals of the $|+Z\rangle$ state ($\mathbf{Q} = \mathbf{M}_2$, order parameter $(0, \phi_2, 0)$), while $(\alpha_{\mathbf{k}}, -\beta_{\mathbf{k}})$ describe the $|-Z\rangle$ state (order parameter $(0, -\phi_2, 0)$). The $|\pm Z\rangle$ states constitute the north and south poles of the pseudospin Bloch sphere, establishing the quantization (\hat{S}^z) axis. Crucially, the orbitals $(\alpha_{\mathbf{k}}, \beta_{\mathbf{k}})$ depend not only on Bloch states, but also on the Coulomb interaction, since they are inferred from linearly superposed many-body ground states. We observe $|\alpha_{\mathbf{k}}| \approx |\beta_{\mathbf{k}}|$ throughout the folded BZ, indicating nearly equal-weight superpositions of \mathbf{k} and $\mathbf{k} + \mathbf{M}_2$ modes in the $|+Z\rangle$ state. This ensures approximate orthogonality $\langle +Z | -Z \rangle \approx 0$, consistent with opposite pseudospin orientations. With the pseudospin basis constructed, the generic ferromagnetic many-body state has the form

$$\Phi(\varphi, \phi) = \prod_{\mathbf{k} \in \text{folded BZ}} \left(\cos \frac{\varphi}{2} \tilde{\phi}_{0,\mathbf{k}}^\dagger + \sin \frac{\varphi}{2} e^{i\phi} \tilde{\phi}_{1,\mathbf{k}}^\dagger \right) |\text{Vac}\rangle, \quad (\text{S12})$$

where the Bloch sphere angle (θ, ϕ) is linked to the CDW order parameters (ϕ_1, ϕ_2, ϕ_3) defined in Eq. (S7).

For all N_g ground states, we compute the $N_g \times N_g$ matrix representations of the pseudospin operators $\hat{S}^{x,y,z}$. A crucial U(1) gauge freedom exists in the orbital definition: $\tilde{\phi}_{1,\mathbf{k}}^\dagger \rightarrow e^{i\Theta_{\mathbf{k}}} \tilde{\phi}_{1,\mathbf{k}}^\dagger$. While this transformation leaves \hat{S}^z eigenvalues (as shown in the main text) unchanged, it affects \hat{S}^x and \hat{S}^y . We fix this gauge by optimizing the phases $\Theta_{\mathbf{k}}$ to maximize the highest eigenvalue of \hat{S}^x , effectively aligning the pseudospin x -axis consistently across the folded Brillouin zone. Once the highest eigenvalue of \hat{S}^x is optimized, highest eigenvalue of \hat{S}^y is also optimized since there is no residual gauge degree of freedom in the pseudospin basis.

The resulting eigenvalues of $\hat{S}^{x,y,z}$ at various w_{AA} are shown in Fig. S4. In the chiral limit ($w_{AA} = 0$), these eigenvalues are approximately quantized and distributed between $-N_p/2$ and $N_p/2$. The slight deviation from exact quantization (e.g., maximum $S^z < N_p/2$) stems from imperfect orthogonality between the north pole ($|+Z\rangle$) and south pole ($|-Z\rangle$) orbital sets. Nevertheless, the near-integer quantization demonstrates approximate SU(2) pseudospin ferromagnetism with total spin $S = N_p/2$, where N_p is the number of pseudospin sites (equal to the number of \mathbf{k} -points in the reduced Brillouin zone). This emergent symmetry persists away from the chiral limit, with comparable quantization quality until $w_{AA}/w_{AB} \approx 0.9$. Beyond this point ($w_{AA}/w_{AB} > 0.9$), the eigenvalues collapse into a continuous distribution, indicating destruction of ferromagnetic order. This abrupt change suggests a quantum phase transition near $w_{AA}/w_{AB} \approx 0.9$.

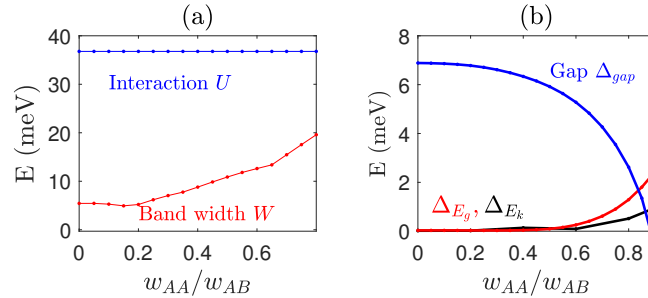


FIG. S5. Hamiltonian energy scales and ground state energy splitting at $\nu_{\text{total}} = 3 + 1/2$ on the $N_s = 28$ cluster. (a) shows the bandwidth and typical Coulomb interaction strength. (b) shows the many-body spectrum gap Δ_{gap} , the total energy splitting Δ_{E_g} between the N_g ground states (red), and the kinetic energy $H_0 = \sum_{\mathbf{k}} \epsilon_{\mathbf{k}} \hat{n}_{\mathbf{k}}$ splitting Δ_{E_k} between the N_g ground states (black).

C. Energy splitting of ground states

Aside from pseudospin ferromagnetism, the emergent SU(2) symmetry manifests through suppressed ground-state energy splitting. Figure S5(a) shows the characteristic Coulomb energy scale U and bandwidth W at total filling

$\nu_{\text{total}} = 3 + 1/2$. The bandwidth increases with w_{AA}/w_{AB} , reaching $W \approx 15$ meV at $w_{AA}/w_{AB} = 0.6$. We estimate the Coulomb scale as $U = V(|\mathbf{G}_1|)N_s/(2A) \approx 40$ meV (for dielectric constant $\epsilon = 4$), where A/N_s is the moiré unit cell area and $|\mathbf{G}_1|$ is the reciprocal lattice vector magnitude. Figure S5(b) displays three key energy scales: (i) many-body excitation gap $\Delta_{\text{gap}} = E_{N_g} - E_{N_g-1}$, (ii) ground-state splitting $\Delta_{E_g} = E_{N_g-1} - E_0$ (energy spread within the N_g -fold manifold), and (iii) kinetic energy variance Δ_{E_k} ($H_0 = \sum_{\mathbf{k}} \epsilon_{\mathbf{k}} \hat{n}_{\mathbf{k}}$ spread). The gap Δ_{gap} closes near $w_{AA}/w_{AB} \approx 0.9$, consistent with the critical point identified from pseudospin quantization (Fig. S4). Remarkably, for $w_{AA}/w_{AB} < 0.6$, Δ_{E_g} remains strongly suppressed (~ 0.1 meV) compared to the bandwidth $W \sim 5 - 15$ meV. Similarly, Δ_{E_k} is suppressed to a similar magnitude, evidenced by nearly identical momentum distributions across the N_g ground states [Figs. S2(a)-(d)]. This suppression of energy splitting demonstrates that the SU(2) symmetry is surprisingly robust and approximately manifests across a significant parameter range away from the chiral limit.

IV. FURTHER NUMERICAL ANALYSIS FOR THE FRACTIONAL CHERN INSULATOR

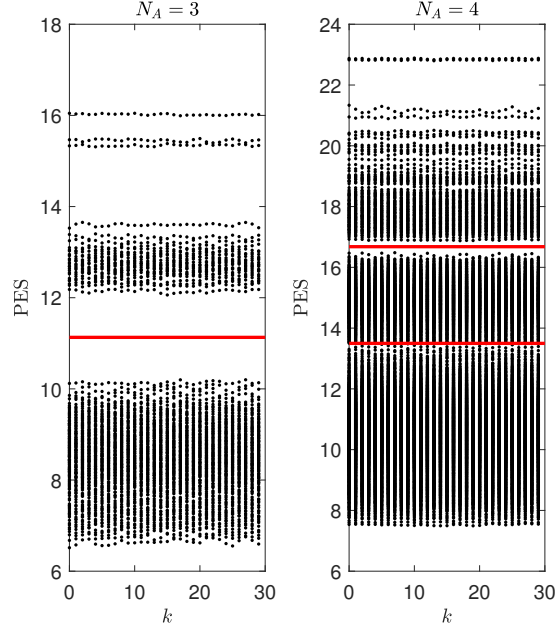


FIG. S6. Particle entanglement spectrum (PES) for $\nu_{\text{total}} = 3 + 1/3$, $N_s = 30$, $w_{AA} = 0.3w_{AB}$ with different subsystem particle number $N_A = 3$ and 4. For $N_A = 3$, the number of states below the PES gap is 3250. For $N_A = 3$, the number of states below the two PES gaps are 17250 and 24840.

To identify the topological order of the fractional Chern insulator at $\nu = 1/3$, we compute the particle entanglement spectrum (PES) [S4] which is defined by eigenvalues of the reduced density matrix in the orbital occupation number basis. The level counting of the PES reflects a generalized Pauli principle that provides a fingerprint for distinguishing different fractional quantum Hall states. For $w_{AA} = 0.3w_{AB}$, we show the PES with subsystem particle numbers $N_A = 3$ and 4 in Fig. S6. The number of states below the PES gaps that separate the low- and higher-energy excitations all match with the Halperin (112) state [S2, S5]. For $w_{AA} = 0.6$, we find that the PES gap is only clear for $N_A = 3$. Nevertheless, we believe that $w_{AA} = 0.6$ and $w_{AA} = 0.3$ belong to the same phase for $\nu_{\text{total}} = 3 + 1/3$ since the many-body spectrum gap is nearly constant in this parameter range.

V. PAIR CORRELATION FUNCTIONS

In the main text only momentum space structure factors are shown. Here we provide further real space pair correlation functions to further confirm symmetry broken/unbroken orders of different phases. The real space pair correlation function is defined as [S6]

$$g(\mathbf{r} - \mathbf{r}') = \frac{1}{N_p^2} \sum_{\mathbf{q}} \langle : \tilde{\rho}_{\mathbf{q}} \tilde{\rho}_{-\mathbf{q}} : \rangle e^{i\mathbf{q}(\mathbf{r} - \mathbf{r}')} \quad (\text{S13})$$

The values of $g(r - r')$ in Fig. S7—for three different fillings—form a periodic pattern with period N_s due to finite discretization of the momentum grid. The yellow circles at $r \approx r'$ correspond to minima, reflecting the repulsive nature of the Coulomb interaction. Away from $r \approx r'$, uniform crystal structures can be recognized with unit cell areas $\sqrt{3}a_M \times \sqrt{3}a_M$, $2a_M \times 2a_M$, and $a_M \times a_M$ in the three cases, respectively. The elementary lattice vectors of each state are labeled by green arrows. For the quantum Hall ferromagnet at $\nu_{\text{total}} = 3 + 1/2$, we clarify that the 2×2 enlarged moiré cell is a consequence of averaging over extensive ground states, as we have seen that different linear combinations from the degenerate ground states yield different ordering wavevectors \mathbf{Q} .

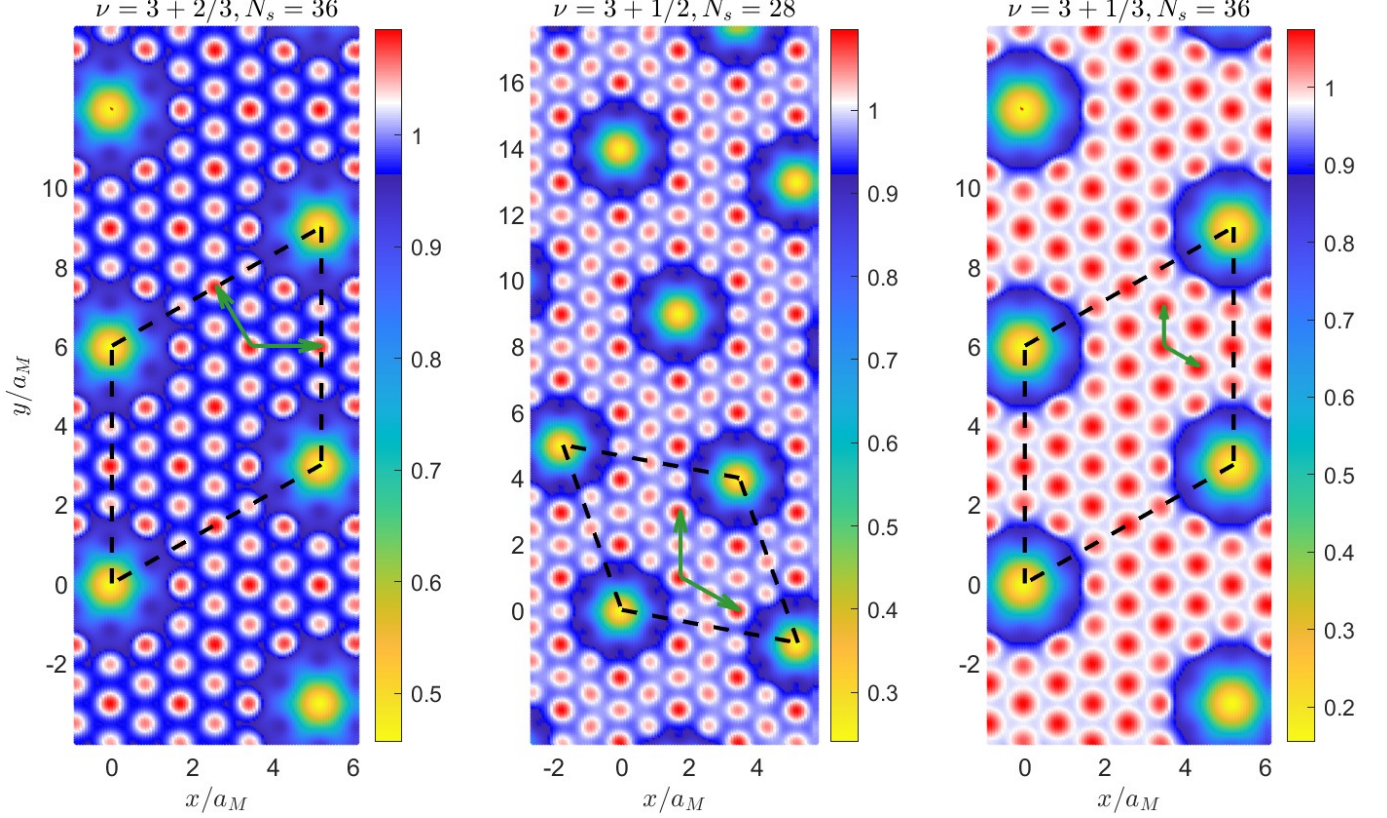


FIG. S7. Real space pair correlation functions $g(r - r')$ for $w_{AA}/w_{AB} = 0.6$ at three filling fractions. The black dashed lines marks the periodic real space clusters of size N_s . The lattice vectors of each state are marked by green arrows.

-
- [S1] D. Guerci, Y. Mao, and C. Mora, Chern mosaic and ideal flat bands in equal-twist trilayer graphene, *Physical Review Research* **6**, L022025 (2024).
 - [S2] J. Dong, P. J. Ledwith, E. Khalaf, J. Y. Lee, and A. Vishwanath, Many-body ground states from decomposition of ideal higher chern bands: Applications to chirally twisted graphene multilayers, *Physical Review Research* **5**, 023166 (2023).
 - [S3] P. Wilhelm, T. Lang, M. S. Scheurer, and A. Läuchli, Non-coplanar magnetism, topological density wave order and emergent symmetry at half-integer filling of moiré chern bands, *SciPost Physics* **14**, 040 (2023).
 - [S4] N. Regnault and B. A. Bernevig, Fractional chern insulator, *Physical Review X* **1**, 021014 (2011).
 - [S5] Y. Liu and Z. Zhu, Engineering fractional chern insulators through periodic strain in monolayer graphene and transition metal dichalcogenides, *arXiv preprint arXiv:2407.12411* (2024).
 - [S6] A. P. Reddy and L. Fu, Toward a global phase diagram of the fractional quantum anomalous hall effect, *Physical Review B* **108**, 245159 (2023).